Electronic Supporting Information for:

Engineering Oxygen-containing and Amino Groups into Two-dimensional Atomically-thin Porous Polymeric Carbon Nitride for Enhanced Photocatalytic Hydrogen Production

Nannan Meng,[†a] Jian Ren,[†bc] Yang Liu,[d] Yi Huang,[a] Tristan Petit*[b] and Bin Zhang*[a]

[a.] Department of Chemistry, School of Science, and Tianjin Key Laboratory of Molecular Optoelectronic Science, Tianjin University, and Collaboration Innovation Centre Science and Engineering (Tianjin), Tianjin 300072, China. E-mail: bzhang@tju.edu.cn

[b.] Methods for Material Development, Helmholtz-Zentrum Berlin für Materialien und Energie GmbH (HZB), Albert-Einstein-Strasse 15, 12489 Berlin, Germany. E-mail: tristan.petit@helmholtz-berlin.de

[c.] Department of Physics, Freie Universität Berlin, Arnimallee 14, 14195 Berlin, Germany

[d.] Analysis and testing center, Tianjin University, Tianjin 300072, China

1. Experimental Procedures

1.1 Preparation of bulk carbon nitride (CNB)

CNB was synthesized by the thermal-polymerization of melamine. In a typical procedure, 5 g of melamine powder was placed in a porcelain boat with a cover and subsequently heated to 500 °C for 2 h, then to 520 °C for another 2 h at the fixed heating rate of 2 ˚C min^{-1}. The obtained product was ground into powder using an agate mortar for further use.

1.2 Preparation of oxygen-containing and amino groups functional carbon nitride atomically-thin porous sheets (CNPS-NH_2)

CNPS-NH_2 was synthesized by the oxidation etching and grafting exfoliation strategies of CNB. In a typical procedure, the as-prepared CNB was placed in the porcelain boat and then transferred into a tube furnace. Firstly, the sample was heated to 520 °C and held for 8 h with a ramp rate of 2 °C min^{-1} under the flowing air (200 scc min^{-1}), and then the sample was treated under NH_3 atmosphere for another 1 h with the heating temperature and gas flow rate remaining constant. After cooling to room temperature, the final product was yielded and abbreviated as CNPS-NH_2. The porous oxygen-rich carbon nitride nanosheets (CNPS-O) were synthesized under the same procedure as CNPS-NH_2 without the NH_3 treatment stage.

1.3 Characterization

Scanning electron microscope (SEM, Hitachi S-4800), Transmission electron microscope (TEM, Philips Tecnai G2 F20) and Atomic force microscopy (AFM, Agilent 5500) were employed to observe the morphologies of the samples. X-ray powder diffraction (XRD, Bruker D8 Focus) was carried out to obtain the crystal phase information. Attenuated total reflectance Fourier-transform infrared (ATR-FTIR, Bruker VERTEX 70v) spectroscopy was used to obtain the information of the different functional groups. X-ray photoelectron spectroscopy (XPS, Perkin-Elmer PHI-1600 spectrometer (Al Kα)) was used to analyze the chemical composites. UV–Vis absorption spectroscopy (Shimadzu UV-2700) and photoluminescence spectroscopy (PL, Jobin Yvon Fluorolog-3-21) were conducted to investigate the optical properties of the samples. Quantachrome Autosorb-iQ2-MP was used to obtain N_2 adsorption/desorption curves and determine the specific surface areas and pore

size distributions of the samples. Time resolved fluorescence measurement (Horiba XH2612) was employed to detect the fluorescence lifetimes of the samples.

1.4 Synchrotron-based soft X-ray absorption spectroscopy

X-ray absorption spectroscopy measurements were performed on solid samples drop casted on conductive Si wafer. The data were collected at the U49/2 PGM1 beamline of the BESSY II synchrotron radiation source using the LiXEdrom endstation. The beamline is connected to an undulator and equipped with plane grating that offers soft X-rays from 85 to 1600 eV with a typical photon flux of 10^{13} photons/s and a resolution (E/ΔE) better than 2.5 × 10^4 below 500 eV. The XAS were measured in the total electron yield (TEY) mode by scanning the samples in the energy range of 276–310 eV (for C K-edge) or 395–420 eV (for N K-edge) in 0.1 eV steps. The XAS spectra in the figures have been normalized to the background before and after the main features.

1.5 Photoelectrochemical experiments

Photoelectrochemical experiments were measured in a conventional three-electrode cell system using an electrochemical workstation (CHI 660D, Shanghai CH Instruments., Inc), where the as-prepared samples, Pt foil and saturated calomel electrode were used as work electrode, counter electrode and reference electrode, respectively. The work electrode was fabricated by using the following typical procedure: 5 mg of sample was dispersed in 50 mL of isopropanol including 2.5 mg $Mg(NO_3)_2·6H_2O$. The clean fluorine-doped tin oxide (FTO, 1 × 2.5 cm^2) was put into above suspension. Then, the applied voltage and deposition time of electrophoresis were set as 60 V and 20 s, respectively. After natural dryness at room temperature, the FTO working electrode was immersed in 0.2 M Na_2SO_4 electrolyte and illuminated from the back side under the 300 W Xe lamp. The light on/off photocurrent response was recorded at each 20 seconds. Electrochemistry impedance spectroscopy (EIS) was performed under the frequency range of 5 mHz to 100 kHz with 10 mV amplitude.

1.6 Photocatalytic experiments

The photocatalytic hydrogen evolution activities of samples were evaluated under the 300 W Xe lamp irradiation (PLS-SXE 300C, Beijing PerfectLight Technology Co., Ltd) equipped with a 420 nm cutoff filter. The produced hydrogen was collected in a gas generation facility (LabSolar-6A, Beijing PerfectLight Technology Co., Ltd) and detected by an online gas chromatograph (Agilent 7890A, Agilent Technologies Technology Co., Ltd) equipped with a thermal conductive detector (TCD) using Ar as a carrier gas. Specifically, 30 mg of catalyst was

homogeneously dispersed into 30 mL of TEOA aqueous solution (3 v/v% TEOA worked as hole scavenger). Subsequently, optimized 3 wt% Ni served as a cocatalyst was loaded on the sample via *in-situ* photodeposition approach with $NiCl_2•6H_2O$ as the precursor of Ni. After degassing treatment of blending dispersion, the sealed quartz cell was top-irradiated under visible light. The reaction temperature was maintained at ambient temperature via a flow of cooling water during the photoredox reaction. The samples with 3 wt% Pt functioned as a cocatalyst were also testified by following the same operation conditions except for the replacement of $NiCl_2•6H_2O$ with $H_2PtCl_6•6H_2O$.

2. Result and Discussion

2.1 The photographs of CNB, CNPS-O and CNPS-NH_2

As can be seen from Figure S1, the as-prepared CNPS-NH_2 sample is loose and lightweight. The bulk density of CNPS-NH_2 is calculated to be about 12 mg cm^{-3}, which is much lower than that of CNB (544 mg cm^{-3}) and CNPS-O (134 mg cm^{-3}). This typical macroscopic ultralight and loose structure will bring about abundant active sites and high solvent accessible surface area at the micro level.

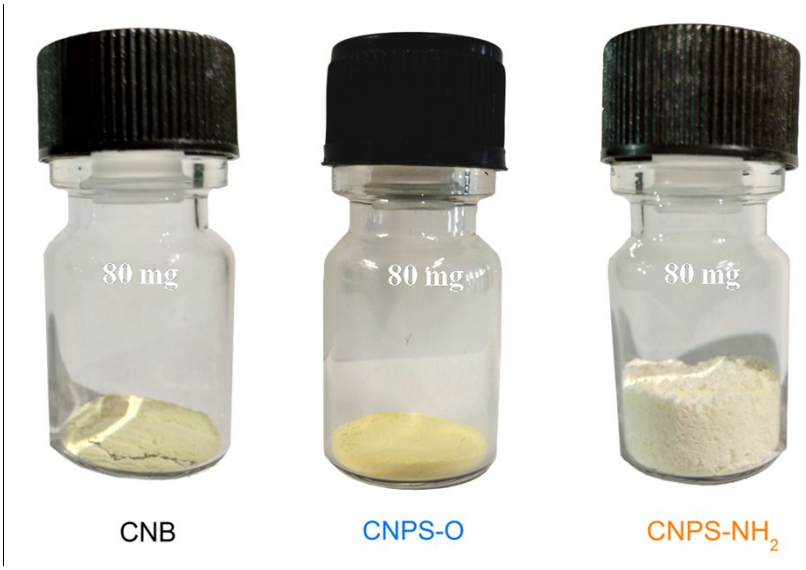

Figure S1. The photographs of CNB, CNPS-O and CNPS-NH_2.

2.2 The TEM images of CNB, CNPS-O and CNPS-NH_2

The TEM images (Figure S2) reveal the stacked morphology of CNB, the pore-rich structure of CNPS-O and the exfoliated CNPS-NH_2 nanosheet. Macroscopic TEM images of CNB, CNPS-O and CNPS-NH_2 displayed in Figure S2a-c further support the result of SEM observations. Moreover, lots of pores can be unquestionably founded in CNPS-O and CNPS-NH_2 (Figure S2d and e), implying tri-s-triazine units in CNB framework are efficiently etched by the oxidation treatment, and the two-dimentional morphology is not destroyed after NH_3-assiated exfoliation.

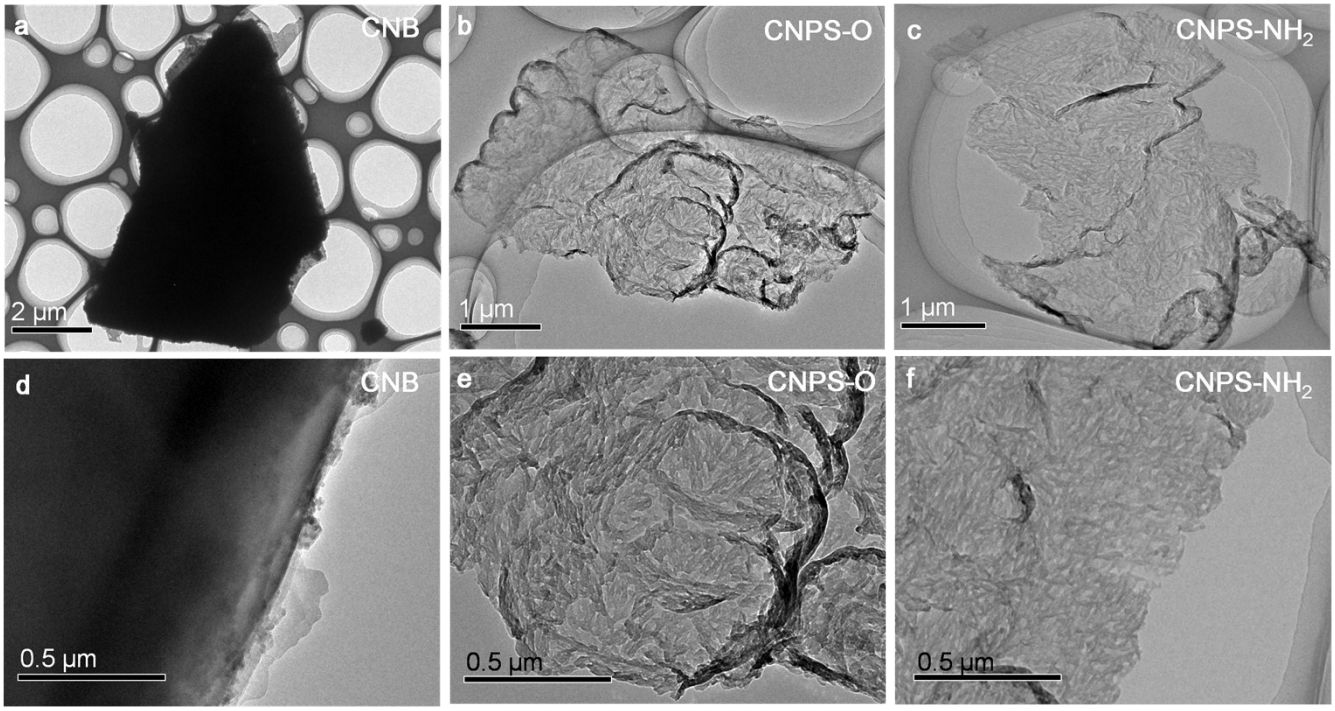

Figure S2. The TEM images of (a, d) CNB, (b, e) CNPS-O and (c, f) CNPS-NH_2.

2.3 The thicknesses of CNPS-O and CNPS-NH_2

As reflected by Figure S3a, the height profile of CNPS-O reflects its thickness is around 9-16 nm. After a further thermal treatment of CNPS-O in NH_3 atmosphere, the thickness is significantly decreased to only 0.4 nm (Figure S3b), suggesting that NH_3-assisted thermal shock exfoliation can efficently destroy the interaction between the neighboring layers. The apparent pores can be observed from the AFM image and the zigzag line of the height profile further support that many pores are decorated on CNPS-NH_2.

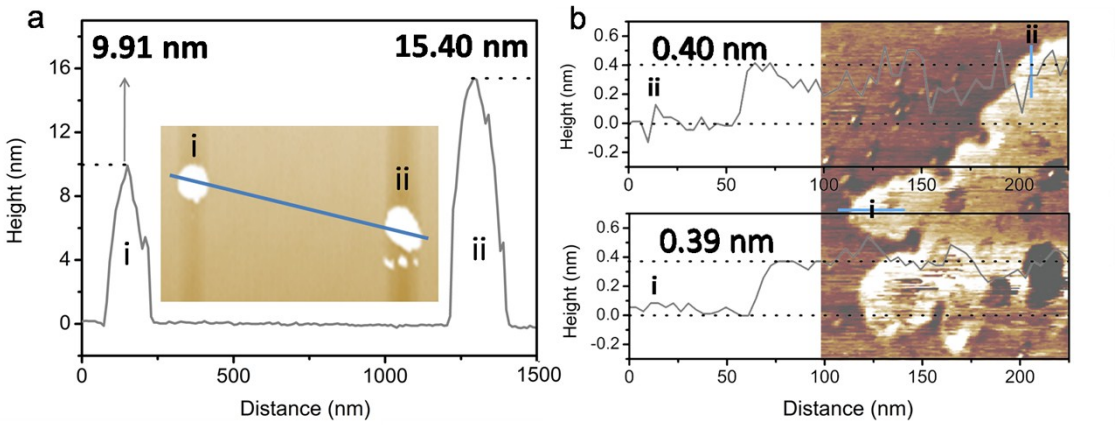

Figure S3. The height profiles of (a) CNPS-O and (b) CNPS-NH_2. The insert is the corresponding AFM image.

2.4 Nitrogen absorption-desorption measurements of the CNB, CNPS-O and CNPS-NH_2

Based on Brunaurer-Emmett-Teller equation, the specific surface area of CNPS-NH_2 is calculated to be 195.3 m^2 g^{-1}, which is higher than that of CNPS-O (48.2 m^2 g^{-1}), and almost 24 times higher than that of CNB (8.2 m^2 g^{-1}).

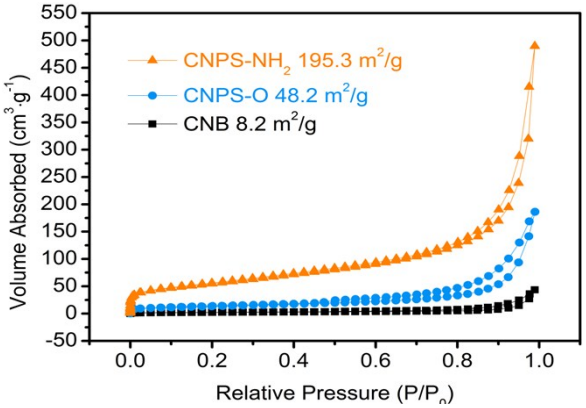

Figure S4. Nitrogen absorption-desorption isotherms of CNB, CNPS-O and CNPS-NH_2.

2.5 Pore structure observation and crystallinity of the CNPS-NH_2

Figure S5a shows that the as-prepared CNPS-NH_2 possesses abundant pores. Selected area electron diffraction (SAED) image of CNPS-NH_2 showed in Figure S5b confirms the amorphous structure of CNPS-NH_2.

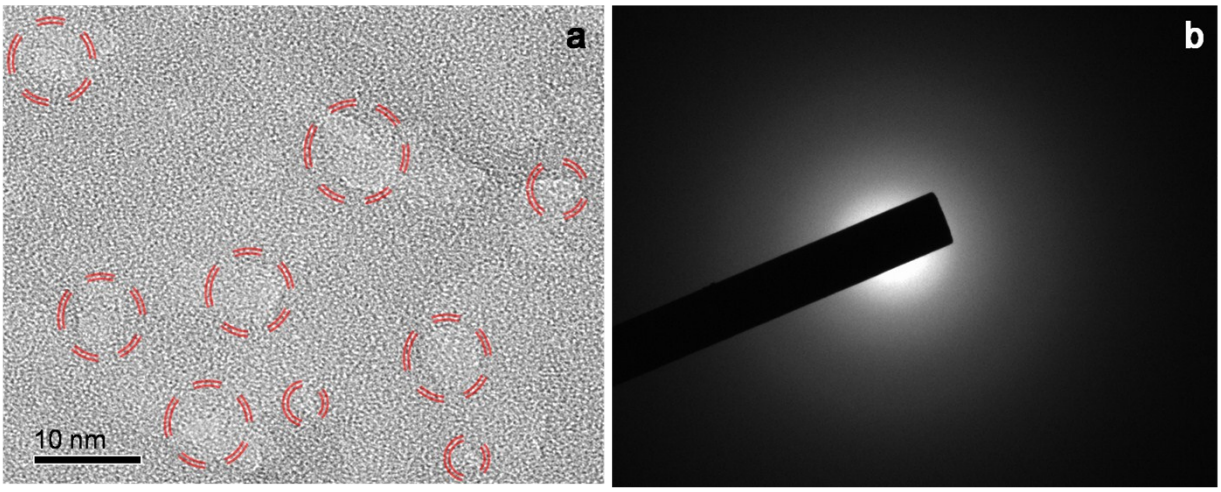

Figure S5. (a) HR-TEM image and (b) SAED image of CNPS-NH_2.

2.6 The ATR-FTIR and Zeta potential measurements of the samples

Full ATR-FTIR spectra corresponding to Figure 1j is showed in Figure S6a. Figure S6b reflects the Zeta potentials of the samples.

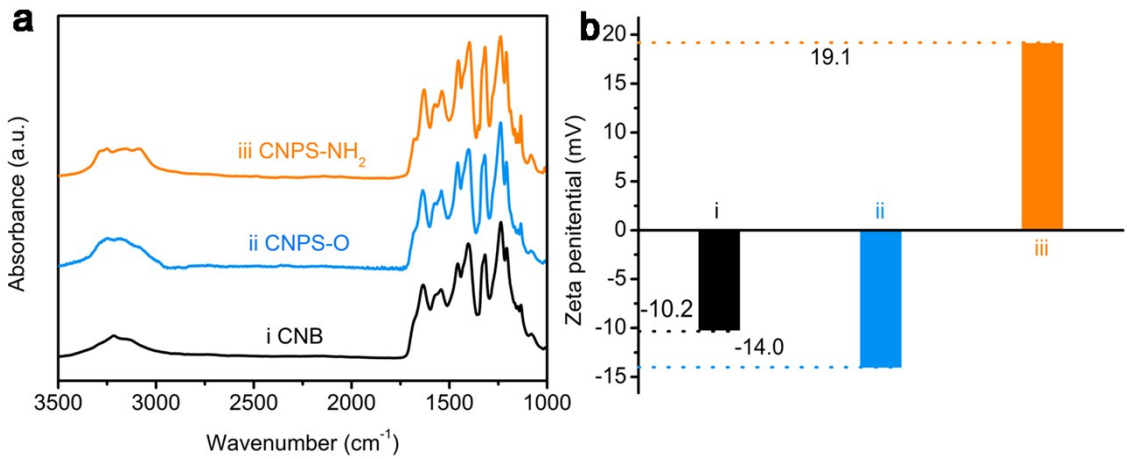

Figure S6. (a) ATR-FTIR spectra and (b) Zeta potentials of CNB, CNPS-O and CNPS-NH_2.

2.7 The contact angle measurements of the samples

The contact angles of CNB, CNPS-O and CNPS-NH_2 are 55.61˚, 40.90˚ and 28.45˚, respectively. The decreasing contact angle demonstrates that the hydrophilicity of the samples can be stepwise improved by the successive two-step thermal treatment.

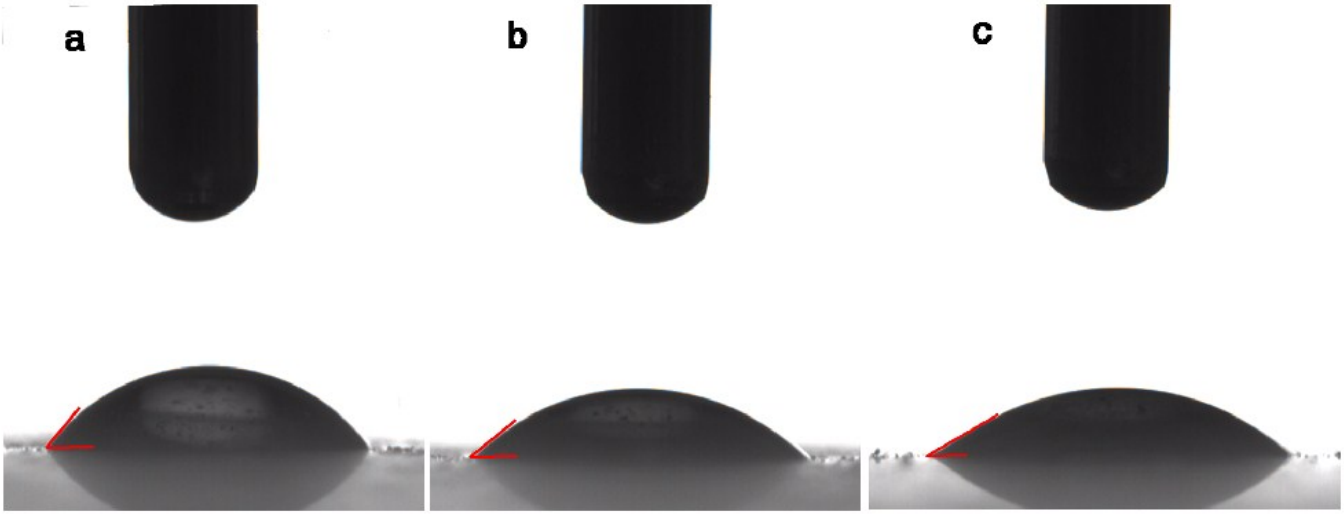

Figure S7. The contact angle measurements of the samples: (a) CNB, (b) CNPS-O and (c) CNPS-NH_2.

2.8 The XPS spectra of the samples

It is can be seen from Figure S8, those samples are all mainly composed of C, N and O elements.

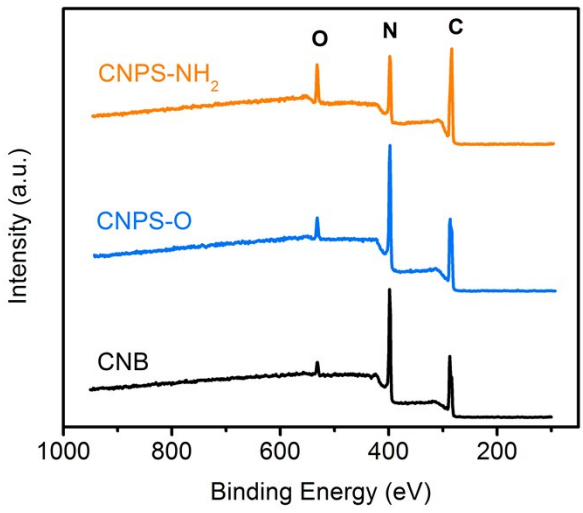

Figure S8. Survey XPS spectra of CNB, CNPS-O and CNPS-NH_2.

2.9 The UV-Vis absorption spectra of samples.

Compared with that of CNB, the red-shift in absorption edge of CNPS-O is observed, which is mainly ascribed to the presence of O-related functional groups. The result is further demonstrated by the increased band gap (Figure S9) and the color change from milky white to yellow (photographs of CNB and CNPS-O displayed in Figure S1). After thermal shock exfoliation of CNPS-O by NH_3, the absorption edge and band gap of CNPS-O do dramatically blue-shift and become larger, respectively. The sample color also changes from yellow to white. Those phenomena are attributed to quantum confinement effect, further demonstrating that CNPS-NH_2 is compose of ultrathin nanosheets.

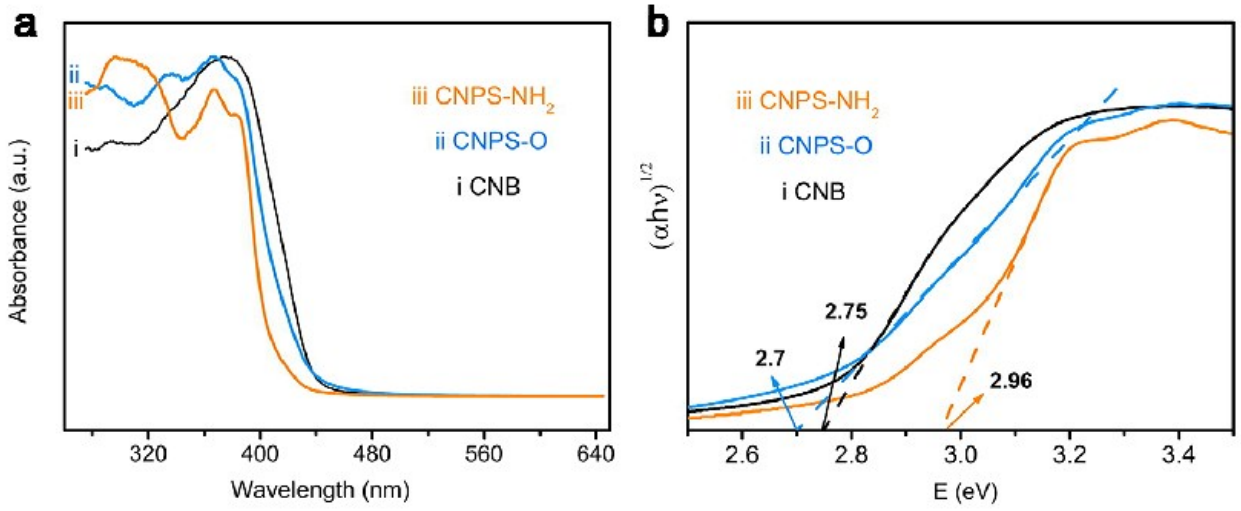

Figure S9. (a) UV-Vis absorption spectra and (b) *αhv* vs. *hv* curves of CNB, CNPS-O and CNPS-NH_2.

2.10 The photoluminescence (PL) spectra of samples

The PL emission peaks of CNB and CNPS-O are shifted from 451 to 459 nm, which is in agreement with the bandgap changing from 2.75 to 2.70 eV (Figure S10). The larger band gap difference between CNPS-O and CNPS-NH_2 is further reflected by the obvious blue-shift of the PL spectra,

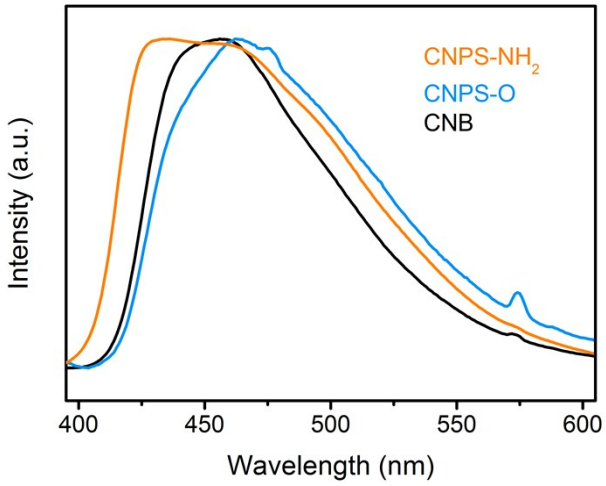

Figure S10. PL spectra of CNB, CNPS-O and CNPS-NH_2.

2.11 The valence-band XPS spectra (VB XPS) of samples

The positions of conduction band and valence band are important for photocatalyst to determine whether photocatalytic reaction can occur. Here, the VB values of CNB, CNPS-O and CNPS-NH_2 respectively corresponding to 1.38, 1.81 1.08 eV are measured by VB XPS spectra (Figure S11).

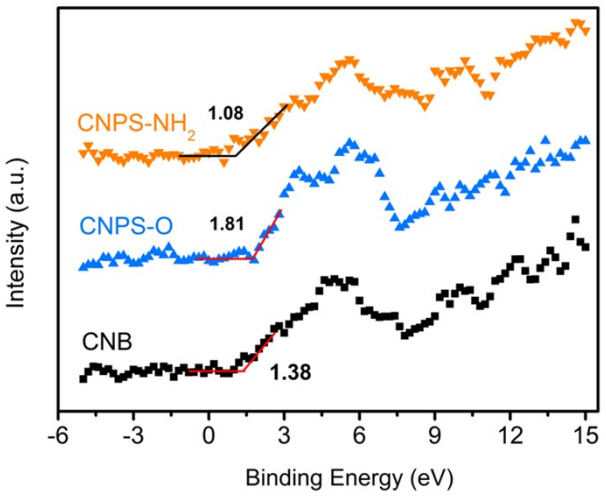

Figure S11. The valence-band XPS spectra of CNB, CNPS-O and CNPS-NH_2.

2.12 Mott-Schottky plots of the CNB and CNPS-NH_2

The CB potentials of CNB and CNPS-NH_2 measured by Mott-Schottky technique (Figure S12) are respectively around -1.42 eV and -1.91 eV. The significantly improved CB potential will provide a huge thermodynamic driving force for the HER. And, those values (the difference value of 0.49 eV) are close to -1.37 and -1.88 eV (the difference value of 0.51 eV) calculated based on the DRS and VB-XPS, indicating these CB potential measured by Mott-Schottky plot is in good agreement with the result calculated from the DRS and VB-XPS.

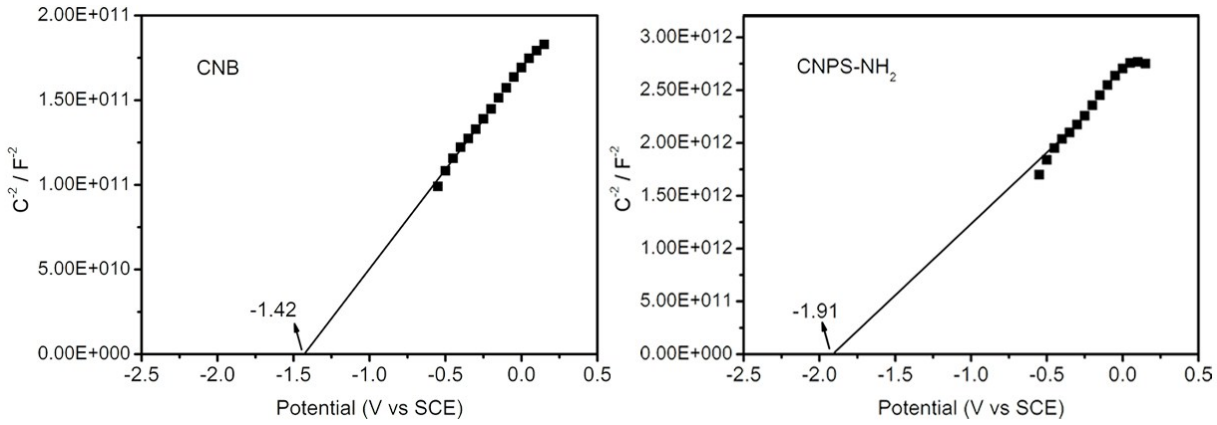

Figure S12. Mott-Schottky plots of the CNB and CNPS-NH_2 Mott-Schottky for CNB and CNPS-NH_2.

2.13 The electrochemical impedance spectra (EIS) of samples

Compared with CNB and CNPS-O, the fast charge separation rate and lower transport impedance of CNPS-NH_2 can be illustrated by its smaller radius of EIS curve (Figure S13).

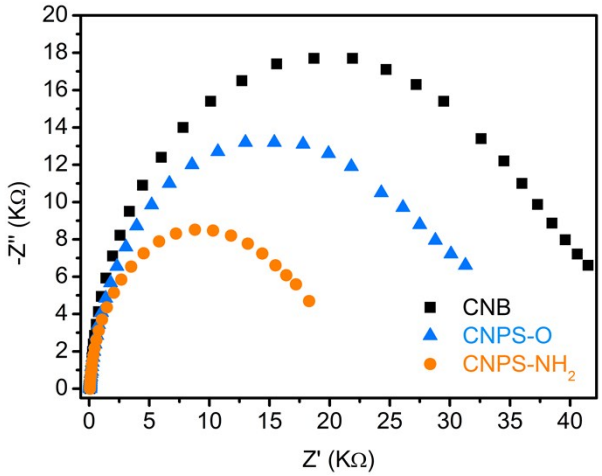

Figure S13. EIS spectra of CNB, CNPS-O and CNPS-NH_2.

2.14 Optimizing hydrogen generation over Ni/CNPS-NH_2 under visible light irradiation

The H_2 evolution activities of CNPS-NH_2 with the presence of different amount of Ni are performed under visible-light irradiation (λ＞420 nm). As can be seen from Figure S14, the photocatalytic H_2 production rate increases with increasing Ni contents up to 3 % and then decrease at higher Ni contents (4 % and 5 %). The lower activity for high Ni content can be attributed to the fact that the excessive amount of Ni deposition leads to the decrease of both the light absorbance ability and active sites.

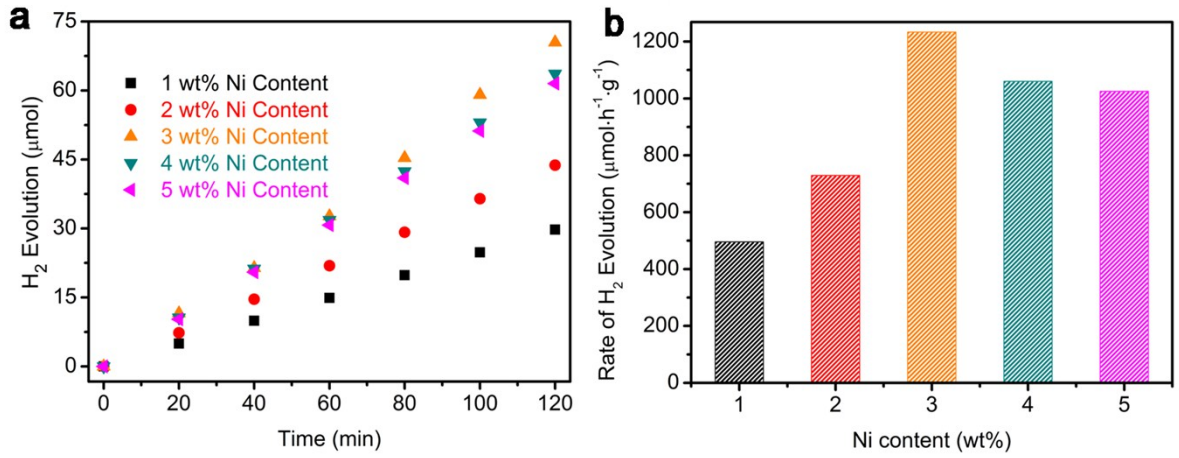

Figure S14. (a) The time courses of H_2 production and (b) the corresponding rates for CNPS-NH_2 with different contents of Ni as cocatalyst.

2.15 The morphology and structure stability of the photocatalyst

As shown in Figure S15a, the pore structure of CNPS-NH_2 is still maintained after several recycling tests, indicating its structural stability. Furthermore, as suggested by XRD patterns of the CNPS-NH_2 before and after cycle testing, the crystalline phase does not change, further suggesting its stable nature (Figure S15c).

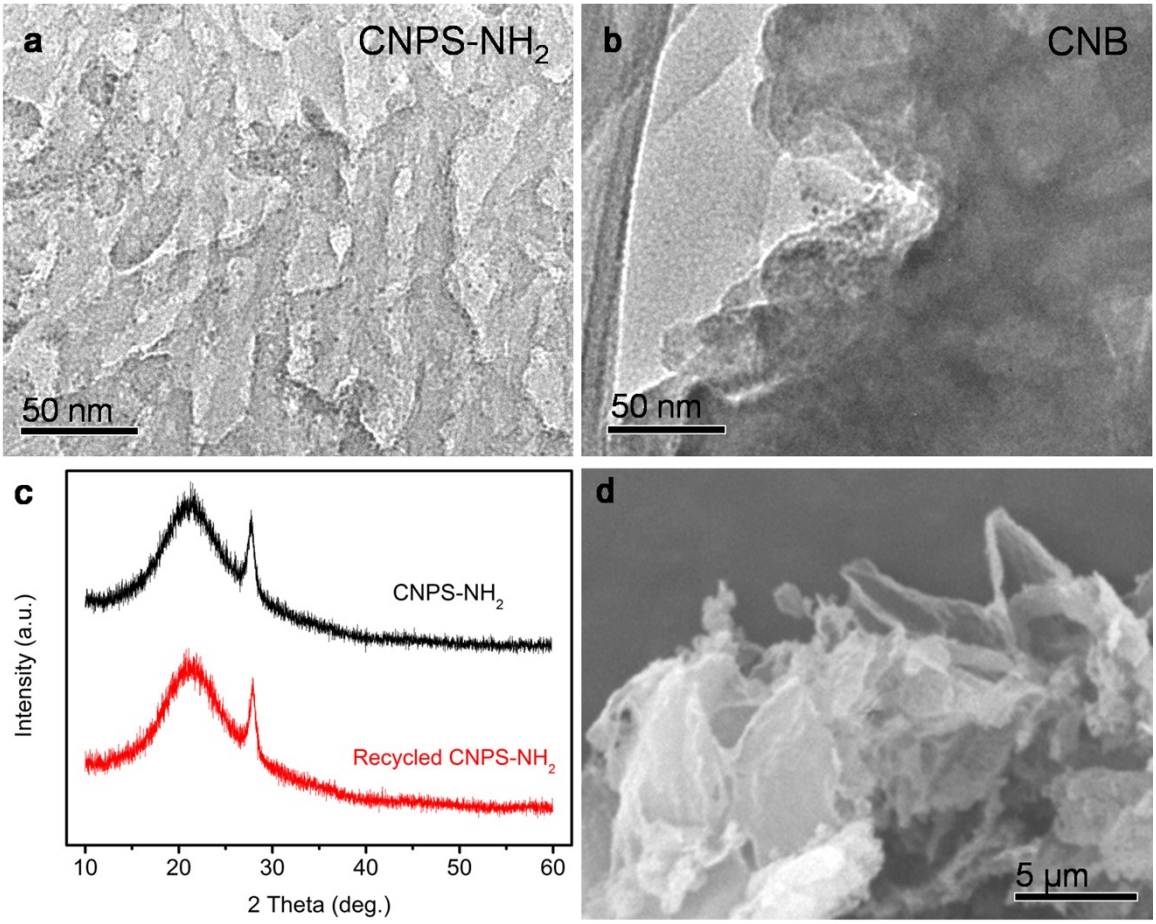

Figure S15. a, b) TEM images of the photocatalysts with 3 wt% Ni as a cocatalyst after long-term photocatalytic test: (a) CNPS-NH_2, (b) CNB. (c) XRD patterns of the fresh and long-term photocatalytic test: CNPS-NH_2. d) SEM image of the recycled CNPS-NH_2.

2.16 Hydrogen generation over the samples with Pt as a cocatalyst

The hydrogen evolution activities of samples with Pt cocatalyst are detected under the visible light and AM1.5 G solar light irradiation (Figure S16). Under visible light irradiation, the H_2 evoluation rates of CNB, CNPS-O and CNPS-NH_2 are 582.7, 2386.5 and 3761.0 μmol h^{-1} g^{-1}, respectivily. And under AM 1.5 G solar irradiation, CNPS-NH_2 yields a H_2 evoluation rate of 20948.6 μmol h^{-1} g^{-1}, which is much better than CNB (5345.8 μmol h^{-1} g^{-1}) and CNPS-O (10956.0 μmol h^{-1} g^{-1}). The visible-light-driven activity is superior than those of previously reported PCN-based materials. In addition, the solar light-responded performance is the best of all the current record PCN photocatalyst as far as we known (Table S1). Based on those results, it is therefore reasonable to infer that the cooperation of precise structure control and surface design can yield the PCN photocatalysts for highly efficient solar-to-fuel energy performance.

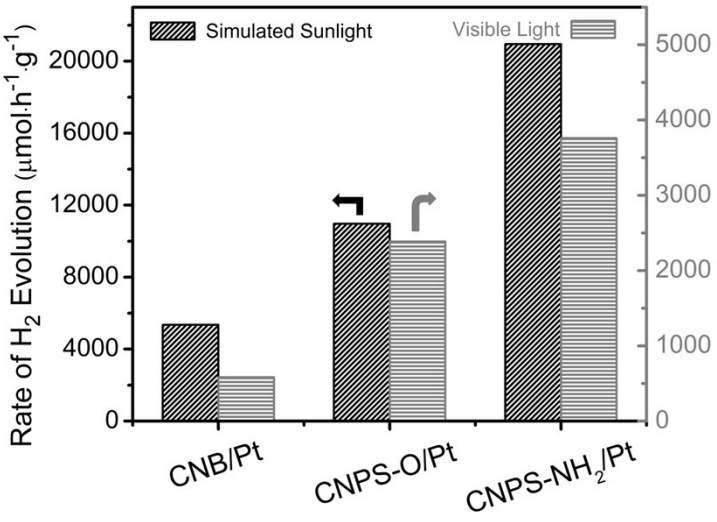

Figure S16. H_2-evolution rates of samples with 3 wt% Pt cocatalyst under visible-light and simulated sunlight irradiation.

Table S1. Comparison of the photocatalytic activity of the as-prepared CNPS-NH_2 with other reported PCN-based photocatalysts.

Samples	H_2 evolution rate (μmol h^{-1} g^{-1})			Cocatalyst	Ref.
	Visible light		Sloar light		
PCN-S	λ＞400	1596	N/A	Pt	[1]
CNS_{650}	λ＞420	2810	N/A	Pt	[2]
ACN	λ＞440	157.9	N/A	Pt	[3]
TSCN	λ＞420	630	N/A	Pt	[4]
PTI nanosheets	λ＞420	1750	N/A	Pt	[5]
IGCNSs	λ＞420	890	N/A	Pt	[6]
CN-580	λ＞440	598	N/A	Pt	[7]
PCN-M	λ＞400	800	N/A	Pt	[8]
UM3	λ＞420	3579	N/A	Pt	[9]
C_3N_4	λ＞420	482	N/A	NiS	[10]
mpg-CN	λ＞420	1030	N/A	MoS_2	[11]
mpg-CN	λ＞420	340	N/A	WS_2	[11]
g-C_3N_4	λ＞400	252	N/A	MoS_2	[12]
g-C_3N_4	λ＞420	1924	N/A	CoP	[13]
g-C_3N_4	λ＞420	82.5	N/A	Ni_2P	[14]
g-C_3N_4	λ＞400	152	N/A	$Ni(OH)_2$	[15]
sg-CN	λ＞420	644	N/A	Ni_2P	[16]
F-CN-96	N/A	N/A	16300	Pt	[17]

Urea-CNx	N/A	N/A	2810	Pt	[18]
PC1.5	N/A	N/A	154.06	Pt	[19]
g-C_3N_4 (urea)	λ＞395	3327.5	20000	Pt	[20]
CNPS-NH_2	**λ＞420**	**1233.5**	**8434.1**	**Ni**	**This Work**
CNPS-NH_2	**λ＞420**	**3761**	**20948.6**	**Pt**	**This Work**

References

[1] J. R. Ran, T. Y. Ma, G. P. Gao, X. W. Du, S. Z. Qiao, *Energy Environ. Sci.,* 2015, **8**, 3708-3717.

[2] J. S. Zhang, J. H. Sun, K. Maeda, K. Domen, P. Liu, M. Antonietti, X. Z. Fu and X. C. Wang, *Energy Environ. Sci.*, 2011, **4**, 675-678.

[3] Y. Kang, Y. Yang, L. C. Yin, X. Kang, G. Liu and H. M. Cheng, *Adv. Mater.,* 2015, **27**, 4572-4577.

[4] Z. W. Tong, D. Yang, Z. Li, Y. H. Nan, F. Ding, Y. C. Shen and Z. Y. Jiang, *ACS Nano*, 2017, **11**, 1103-1112.

[5] K. Schwinghammer, M. B. Mesch, V. Duppel, C. Ziegler, J. Senker and B. V. Lotsch, *J. Am. Chem. Soc.,* 2014, **136**, 1730-1733.

[6] Q. Han, C. G. Hu, F. Zhao, Z. P. Zhang, N. Chen and L. T. Qu, *J. Mater. Chem. A.,* 2015, **3**, 4621-4619.

[7] Y. Y. Kang, Y. Q. Yang, L. C. Yin, X. D. Kang, L. Z. Wang, G. Liu and H. M. Cheng, *Adv. Mater.,* 2016, **28**, 6471-6477.

[8] P. J. Yang, H. H. Ou, Y. X. Fang and X. C. Wang, *Angew. Chem. Int. Ed*., 2017, **56**, 3992-3996.

[9] N. Tian, Y. H. Zhang, X. W. Li, K. Xiao, X. Du, F. Dong, G. I. N. Waterhouse, T. R. Zhang and H. W. Huang, *Nano Energy,* 2017, **38**, 72-81.

[10] J. D. Hong, Y. S. Wang, Y. B. Wang, W. Zhang and R. Xu, *ChemSusChem,* 2013, **6**, 2263-2268.

[11] Y. D. Hou, A. B. Laursen, J. S. Zhang, G. G. Zhang, Y. S. Zhu, X. C. Wang, S. Dahl and I. Chorkendorff, *Angew. Chem. Int. Ed.,* 2013, **52**, 3621-3625.

[12] H. Zhao, Y. M. Dong, P. P. Jiang, H. Y. Miao, G. L. Wang and J. J. Zhang, *J. Mater. Chem. A.,* 2015, **3**, 7375-7381.

[13] C. M. Li, Y. H. Du, D. P. Wang, S. M. Yin, W. G. Tu, Z. Chen, M. Kraft, G. Chen and R. Xu, *Adv. Funct. Mater.,* 2017, **27**, 1604328.

[14] P. Ye, X. L. Liu, J Locozzia, Y. P. Yuan, L. N. Gu, G. S. Xu and Z. Q. Lin, *J. Mater. Chem. A.,* 2017, **5**, 8493-8498.

[15] J. G. Yu, S. H. Wang, B. Cheng, Z. Lin and F. Huang, *Catal. Sci. Technol.* 2013, **3**, 1782-1789.

[16] A. Indra, A. Acharjya, P. W. Menezes, C. Merschjann, D. Hollmann, M. Schwarze, M. Aktas, A. Friedrich, S. Lochbrunner, A. Thomas and M. Driess, *Angew. Chem. Int. Ed.,* 2017, **56**, 1653-1657.

[17] H. Wang, X. D. Zhang, J.F. Xie, J.J. Zhang, P. Ma, B. C. Pan and Y. Xie, *Nanoscale,* 2015, **7**, 5152-5156.

[18] V. W. Lau, V. W. Yu, F. Ehrat, T. Botari, I. Moudrakovski, T. Simon, V. Duppel, E. Medina, J. Stolarczyk, J. Feldmann, V. Blum and B. V. Lotsch, *Adv. Energy. Mater.,* 2017, **7**, 1602251.

[19] Y. Sui, J. H. Liu, Y. W. Zhang, X. K. Tian and W. Chen, *Nanoscale,* 2013, **5**, 9150-9155.

[20] D. J. Martin, K.P. Qiu, S. A. Shevlin, A. D. Handoko, X.W. Chen, Z. X. Guo and J. W. Tang, *Angew. Chem. Int. Ed.,* 2014, **53**, 9240-9245.